**International Journal Of Engineering Research And Development**
e- ISSN: 2278-067X, p-ISSN: 2278-800X, www.ijerd.com
Volume 16, Issue 4 (April 2020), PP. 28-41

# Assessment of Borehole Stability after Pulsed Fracture

Xinyong Li[1], Yujie Wang[2], Bing Zhao[1], Zhennan Zhang[2]
[1]*Research Institute of Petroleum Engineering, Sinopec Northwest Oilfield Branch, Urumqi, Xinjiang, 830011, China*
[2]*School of Naval Architecture, Ocean and Civil Engineering, Shanghai Jiao Tong University, Shanghai, 200240, China*

***Abstract:*** *The pulsed fracture(PF) technique is promising in the reservoir stimulation. Under the high pressurization rate, the fracture branches to form the complex fracture network in reservoir. However, the high pressurization rate may lead to the wellbore instability. To assess the wellbore stability involved in PF, an assessment method is developed based on the numerical simulation and theoretical analysis. A damage factor is developed to assess the residual strength of surrounding rock while the Mohr-Coulomb criterion is used to predict the critical strength. Then wellbore stability is analysed via comparing the residual strength with the critical strength of surrounding rock. The simulation results suggest that the bigger the internal friction angle is, the more safe the wellbore is. It founds that the dangerous area increases with increasing the material modulus. The dangerous area gets larger with the horizontal stress difference increasing. Under the specific peak pressure, the pressurization time has significant impact on the wellbore stability. The proposed method provides a simple and effective assessment method for wellbore stability after PF stimulation.*

***Keywords:*** *Pulsed fracture (PF); Borehole stability; Mohr-Coulomb criterion; Numerical simulation.*

---

Date of Submission: 18-05-2020 Date of Acceptance: 03-06-2020

---

## I. INTRODUCTION

Carbonate reservoir is an important kind of reservoir around the world. However, due to the fracture-cavity structure formed in Karstification process, it is very difficult to exploit via the conventional reservoir stimulation [1, 2]. To overcome this problem, many different techniques have been developed, such as the multilateral well technique [3], the acidized fracturing technique [4, 5], the perforation technique [6, 7] and the pulsed fracturing technique [8-11]. Among these techniques, the pulsed fracture (PF) is a promising one. PF is essentially a dynamic fracture process. Under a high pressurization rate, the multiple fracture can be generated at the wellbore simultaneously, which are connected with the natural fractures to form a complex fracture network in reservoir [12-14]. However, the high pressurization rate applied in the wellbore is a potential threat to the wellbore instability. Before the application of PF, it is quite necessary to conduct an investigation on the wellbore stability by PF. To explore this problem, this paper tries to develop a feasible method on the evaluation of wellbore stability after PF stimulation.

The wellbore stability is closely related to the in-situ stresses, inclined angle, pore pressure, rock properties, stratum structure, and other ambient conditions [15-20]. The failure of the surrounding rock around the wellbore can lead to mud lost, lost circulation, and pipe stucking. The paper mainly focus on the wellbore instability induced by the PF process. In PF stimulation, due to the instantaneous loading and unloading process, the radial tensile stress is prone to induce the disturbance or damage in the surrounding rock of borehole. The disturbed (damaged) zone distributed around wellbore may seriously threaten the wellbore stability.

For the borehole stability, the material behavior affected by the stress distribution surrounding the wellbore is a key point. To efficiently simulate the failure process, the augmented virtual internal bond (AVIB) [21] model is adopted as the constitutive model of the rock matrix. The AVIB intrinsically incorporates the micro fracture mechanism in the macro constitutive relation. It can naturally reproduce the macro failure process of material without any separate fracture criterion. It is convenient and efficient for AVIB method to model the macro failure of material, including the fracture initiation, propagation and branch.

## II. PF SIMULATION METHOD

### 2.1 Mechanical model of material

In this study, the AVIB is adopted for the material mechanical modeling. AVIB is a micro-macro constitutive model [21], which originates from the virtual internal bond (VIB) theory [22]. It considers the material to consist of material particles (Fig. 1a).

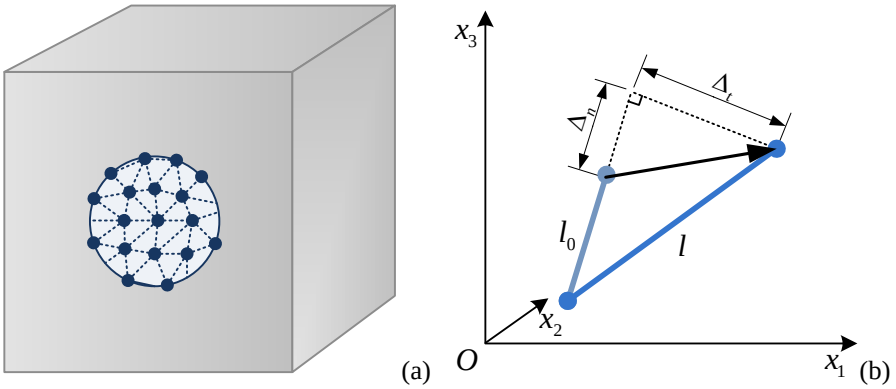


**Fig. 1** Augmented virtual internal bond model: (a) micro configuration; (b) bond deformation.

The interaction between particle is characterized by a cohesive law, which intrinsically includes the fracture mechanism of material at the micro level. So it can naturally reproduce the macro failure of material without any separated fracture criterion. In AVIB, the fixed Poisson ratio problem of original VIB is overcame by taking the Xu-Needleman potential [23, 24] as the bond potential, which reads

$$U(\Delta)=\phi_n-\phi_n\exp\left(-\frac{\Delta_n}{\delta_n}\right)\left[1+\frac{\Delta_n}{\delta_n}\right]\left[1-q+q\exp\left(-\frac{\Delta_t^2}{\delta_t^2}\right)\right] \tag{1}$$

where $\delta_n$ and $\delta_t$ are the characteristic lengths for normal and tangential separations, $\delta_n=\delta_t=\tilde{\varepsilon}_t l_0$; $\tilde{\varepsilon}_t$ is the bond strain at the peak uniaxial tensile force, usually, $\tilde{\varepsilon}_t=\varepsilon_t$ with $\varepsilon_t$ being the strain value at the peak stress of the uniaxial tension stress-strain curve of material; $l_0$ is the undeformed bond length; $\Delta_n$ and $\Delta_t$ are the normal and tangential deformations of bond; the bond energy $\phi_n$ and energy ratio $q$ are related to the macro elastic constants

$$\begin{aligned}\phi_n&=\frac{V\delta_{\mathrm{n}}^2}{l_0^2}\cdot\frac{3E}{4\pi(1-2\nu)}\\ q&=\frac{\delta_{\mathrm{t}}^2}{\delta_{\mathrm{n}}^2}\cdot\frac{(1-4\nu)}{2(1+\nu)}\end{aligned} \tag{2}$$

with $E$ being the Young's modulus; $\nu$ the Poisson's ratio and $V$ the volume of the representative element volume (REV).

According to the Cauchy-Born rule, the bond deformations (Fig. 1b) is related to the macro strain tensor through

$$\begin{aligned}\Delta_n&=\boldsymbol{\xi}^T\boldsymbol{\varepsilon}\boldsymbol{\xi}l_0\\ \Delta_t^2&=\left[\boldsymbol{\xi}^T\boldsymbol{\varepsilon}^T\boldsymbol{\varepsilon}\boldsymbol{\xi}-\left(\boldsymbol{\xi}^T\boldsymbol{\varepsilon}\boldsymbol{\xi}\right)^2\right]l_0^2\end{aligned} \tag{3}$$

where $\boldsymbol{\xi}$ is the unit orientation vector of bond, $\boldsymbol{\xi}=\left[\sin\theta\cos\phi,\ \sin\theta\sin\phi,\ \cos\theta\right]^T$ in the spherical coordinates.

The stress tensor of REV in AVIB has the form

$$\sigma_{ij}=\frac{1}{V}\frac{\partial}{\partial\varepsilon_{ij}}\left\langle U(\Delta_n,\Delta_t)\right\rangle \tag{4}$$

and the tangent modulus tensor

$$C_{ijkl}=\frac{1}{V}\frac{\partial^2}{\partial\varepsilon_{ij}\partial\varepsilon_{kl}}\left\langle U(\Delta_n,\Delta_t)\right\rangle \tag{5}$$

where $\varepsilon_{ij}$ is the strain tensor of REV; the integral operator $\langle\cdots\rangle$ stands for $\langle\cdots\rangle=\int_0^{2\pi}\int_0^{\pi}(\cdots)D(\theta,\phi)\sin\theta\mathrm{d}\theta\mathrm{d}\phi$ with $D(\theta,\phi)$ being the bond distribution density in terms of the spherical coordinates $\theta$ and $\phi$.

In AVIB, the element failure is identified through following criterion

$$\varepsilon_1>\eta\varepsilon \tag{6}$$

where $\varepsilon_1$ is the maximum principal value of REV; $\eta$ is a coefficient and $\eta>1$. In AVIB, it is reasonable to assume that the residual strength of element can be ignored as $\varepsilon_1>5\varepsilon_t$.

### 2.2 Pulsed pressurization modeling

The fracturing process is driven by the internal pulse pressure. Once the fracture is extended, the internal pressure spread further and act on the inner surface of fracture. In this study, the internal pressure is exerted on the fractured element, in which the pressure gradient along fracture is ignored. The same scheme had also been adopted in [12-14, 25]. For the triangular facet of tetrahedron element, the equivalent nodal force caused by internal pressure can be calculated as

$$F_i = \frac{\left(\mathbf{r}_{ij} \times \mathbf{r}_{im}\right)_n}{2n} \bar{P} \tag{7}$$

where $\mathbf{r}_{ij}, \mathbf{r}_{im}$ are the edge vectors of triangular facet; $n$ is the node number of triangular facet.

## III. ASSESSMENT METHOD FOR WELLBORE STABILITY

PF is a promising stimulation technique to generate complex fractures network in reservoir. Under a high pressurization rate, there will be radial fracture generated at the borehole instantaneously (Fig. 2). After that, the stress state of rock matrix changes, which may lead to the borehole instability. To characterize the wellbore stability, the PF simulation under different situations is conducted at first, in which the stress distribution surrounding the wellbore is recorded. Secondly, according to the mechanical state of surrounding rock, the damage factors of the rock surrounding the wellbore are derived. Subsequently, comparing the residual strength with the critical strength derived from analytical value, the risk of wellbore stability is evaluated quantitatively.

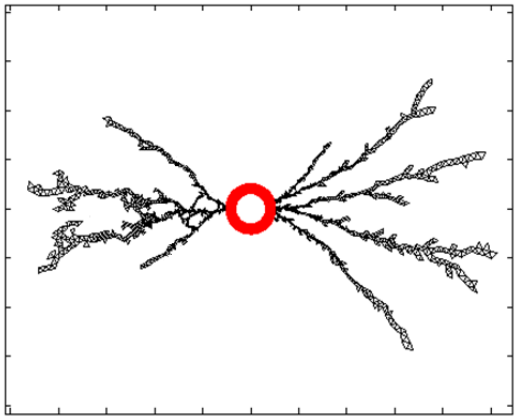

**Fig. 2** Pulsed fractures at wellbore.

### 3.1 Stress field around wellbore

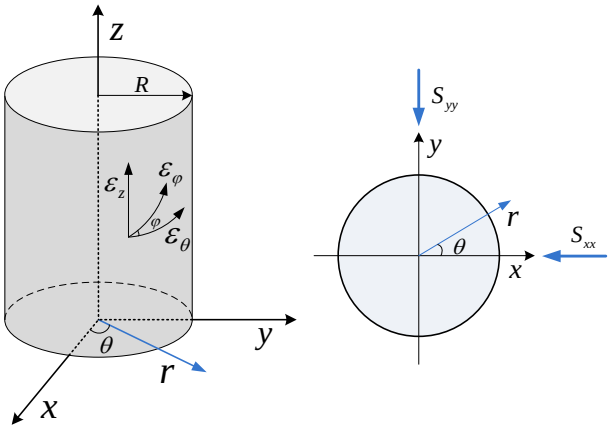


**Fig. 3** Wellbore in cylindrical coordinate system.

To assess the wellbore stability, the analytical solution of surrounding stress of wellbore is adopted for reference. For the circular wellbore, we assume it is subjected to the in-situ stresses shown in Fig. 3. In the cylindrical coordinate system, the stress field around wellbore can be written as [26]

$$\begin{aligned}
\sigma_{rr} &= \frac{1}{2}\left(S_{xx}+S_{yy}\right)\left(1-\frac{R^2}{r^2}\right)+\frac{1}{2}\left(S_{xx}-S_{yy}\right)\left(1-4\frac{R^2}{r^2}+3\frac{R^4}{r^4}\right)\cos 2\theta+\left(P_W-P_p\right)\frac{R^2}{r^2}\\
\sigma_{\theta\theta} &= \frac{1}{2}\left(S_{xx}+S_{yy}\right)\left(1+\frac{R^2}{r^2}\right)-\frac{1}{2}\left(S_{xx}-S_{yy}\right)\left(1+3\frac{R^4}{r^4}\right)\cos 2\theta-\left(P_W-P_p\right)\frac{R^2}{r^2}\\
\sigma_{zz} &= S_{zz}-2\nu\left(S_{xx}-S_{yy}\right)\cos 2\theta-P_p\\
\tau_{r\theta} &= \frac{1}{2}\left(S_{xx}+S_{yy}\right)\left(1+2\frac{R^2}{r^2}-3\frac{R^4}{r^4}\right)\sin 2\theta\\
\tau_{rz} &= \tau_{z\theta}=0
\end{aligned} \tag{8}$$

where $P_W$ is the internal pressure of wellbore; $P_p$ is the pore pressure of formation; $\nu$ is the Poisson ratio of rock matrix. (The stress symbols are assumed as positive in compression and negative in tension.)
Shown in Fig. 4, the stress regime of the matrix around wellbore (in the polar coordinate system) can be derived as

$$\begin{aligned}
\sigma_{rr} &= P_W-P_p\\
\sigma_{\theta\theta} &= \left(S_{xx}+S_{yy}\right)-2\left(S_{xx}-S_{yy}\right)\cos 2\theta-\left(P_W-P_p\right)\\
\sigma_{zz} &= S_{zz}-2\nu\left(S_{xx}-S_{yy}\right)\cos 2\theta-P_p\\
\tau_{r\theta} &= \tau_{rz}=\tau_{\theta z}=0
\end{aligned} \tag{9}$$

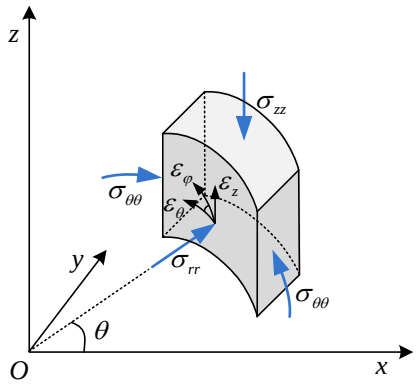


**Fig. 4** The representative element volume of wellbore wall.

### 3.2 Strength of surrounding rock

To evaluate the wellbore stability, the following strength criterion is adopted to characterize the state of surrounding rock, which has the form

$$F\left(\boldsymbol{\sigma},\boldsymbol{\chi}\right)=0 \tag{10}$$

where $\boldsymbol{\sigma}$ is the stress tensor of the arbitrary point on borehole wall; $\boldsymbol{\chi}$ is the parameters set of material strength.
According to the analytical stresses expressions in Eq. (2), the local stresses on the borehole wall evolves with the direction angle. Thus it is necessary to consider the evolution of stress state with direction angle. The minimum strength of surrounding rock is taken as the critical strength. The critical strength curve of surrounding rock is shown in Fig. 5.

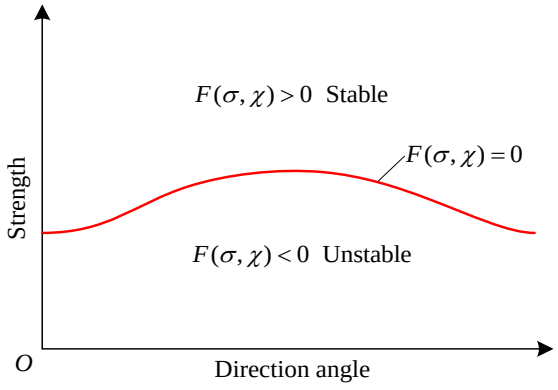

**Fig. 5** Relationship between the residual strength and the critical strength.

Under the disturbance of PF, there will be damaged region formed in the surrounding rock, which may significantly influence the wellbore stability. The damage in surrounding rock can be characterized by the damage degree factor, which can be derived from the results of numerical simulation. To quantify the damage degree caused by fracturing disturbance, we define the damage factor as

$$D=\begin{cases}\dfrac{\varepsilon_1}{\lambda\varepsilon_t} & 0<\varepsilon_1<\lambda\varepsilon_t \\ 1.0 & \varepsilon_1\geq\lambda\varepsilon_t\end{cases} \tag{11}$$

where $\varepsilon_1$ is the maximum principle strain.

According to the damage degree factor, the residual strength of material point can be derived as

$$\chi_R=(1-D)\chi \tag{12}$$

where $\chi_R$ is the residual strength of material point; $D$ is the damage factor, for the fractured material point $D=1.0$. So we can get the curve of residual strength with direction angle.

### 3.3 **Wellbore stability assessment**

Comparing the residual strength with the critical strength (Fig. 5), the possibility of borehole instability is clearly presented. If the residual strength curve is completely above the critical strength curve, the borehole can hold stability after fracturing. Conversely, if the residual strength curve is all or part bellow the critical strength curve, the borehole may be unstable. Further, the stability criterion of wellbore can written as

$$\Gamma_R(\theta)>\Gamma_C(\theta) \tag{13}$$

where $\theta$ is the direction angle; $\Gamma_R(\theta)$ is the residual strength of surrounding rock; $\Gamma_C(\theta)$ is the critical strength of surrounding rock.

## IV. CRITICAL STRENGTH CRITERION

The critical strength criterion can be expressed in terms of the properties of the surrounding rock. In present paper, the Mohr-Coulomb criterion is adopted as the critical strength criterion, which reads

$$\sigma_1-P_p=(\sigma_3-P_p)\cdot\cot^2\left(45^\circ-\frac{\varphi}{2}\right)+2C\cot\left(45^\circ-\frac{\varphi}{2}\right) \tag{14}$$

where $\sigma_1$, $\sigma_3$ are the maximum and minimum principal stress; $C$ is the cohesion of material; $\varphi$ is the internal friction angle.

According to Eq. (6), the critical cohesion strength can be written as

$$C=\frac{\left[(\sigma_1-P_p)-(\sigma_3-P_p)\cdot\cot^2\left(45^\circ-\frac{\varphi}{2}\right)\right]}{2\cdot\cot\left(45^\circ-\frac{\varphi}{2}\right)} \tag{15}$$

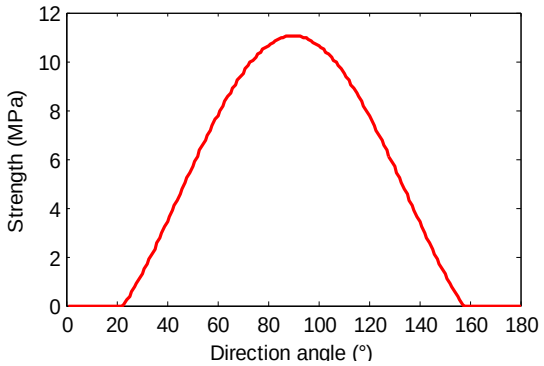


**Fig. 6** Critical strength of the surrounding rock with $\varphi=24.0^\circ$.

Subjected to the in-situ stresses, pore-pressure and internal pressure of wellbore, the components of stress tensor can be derived through stress analysis. Then the critical cohesion strength can be derived via the Eq. (7). For

instance, Fig. 6 shows the critical cohesion strength with internal friction angle $\varphi = 24.0^{o}$, the in-situ stresses $S_x = 130.0$ MPa, $S_y = 120.0$ MPa and $S_z = 115.0$ MPa, the pore pressure of formation $P_p = 0.0$, the pressure at wellbore $P_w = 70.0$ MPa.

## V. SIMULATION CASES

The wellbore stability is closely related to the matrix property, the in-situ stresses, the pressurization pattern and others factors. To clarify the influence of various factors, we conduct the following numerical simulations, where the wellbore stability is analysed through the proposed approach.

### V.1 Effects of material property

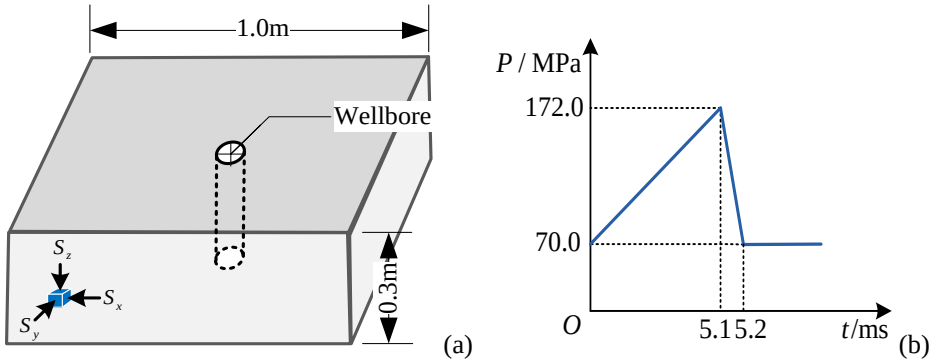


**Fig. 7** Simulation object of the pulsed fracture: (a) simulation object and boundary condition; (b) pressurization scheme.

The stability of surrounding rock is closely related to the material properties. To investigate the critical strength under different material property, we take the internal friction angle as $\varphi = 25.0^{o}$ and $27.0^{o}$, respectively. The simulation domain is a $1.0\text{m} \times 1.0\text{m} \times 0.3\text{m}$ block (shown in Fig. 7a), which is subjected to the in-situ stresses $S_x = 124.5$ MPa, $S_y = 88.0$ MPa and $S_z = 111.5$ MPa. The radius of the centered wellbore in computational domain is $r$=0.1 m. The other parameters of material properties respectively are: the Young's modulus $E = 40.0$ GPa, the Poisson ratio $\nu$=0.2, $\sigma_t = 4.0$MPa, $C = 10.0$ MPa. Fig. 7b shows the pressurization scheme at wellbore. The time step of pressurization adopted in simulation is $\Delta t = 1.0\mu$s. Initially, the pressure is imposed on the inner wall of whole wellbore. The simulation results of PF are shown in Fig. 8.

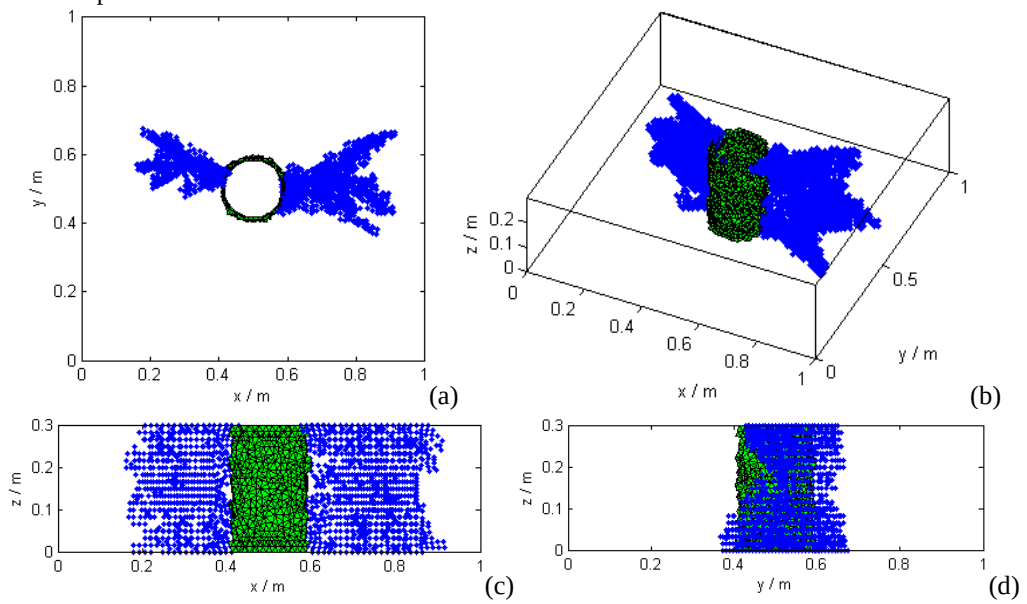


**Fig. 8** Pulsed fracture trajectories in different perspectives at the time t= 5.2 ms.

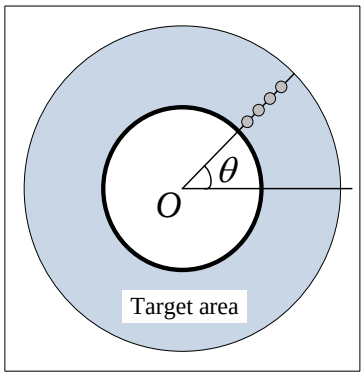


**Fig. 9** The target area of wellbore stability assessment.

Under the pulse pressurization, the fractures initiate at the wellbore and propagate in the direction of horizontal maximum in-situ stress (Fig. 8). Shown in Fig. 9, to facilitate the wellbore stability assessment, we term a finite loop region surrounding the wellbore as 'target area'. Here, we take the external radius of this area $r_{loop} = 0.5$ m. According to the pulsed fracturing simulation, the damage area of the surrounding rock of wellbore is obtained, shown in Fig. 10 (The darker the color, the larger the damage factor.). Comparing the residual strength with the critical strength (shown in Fig. 11), it is found that the internal friction angle has a significant effect on the wellbore stability. The bigger the internal friction angle is, the more safe the wellbore is.

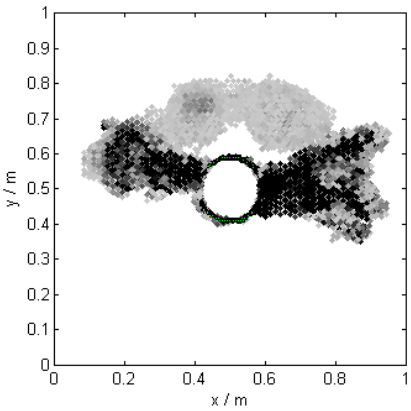


**Fig. 10** Damage distribution of the surrounding rock (t= 5.2 ms).

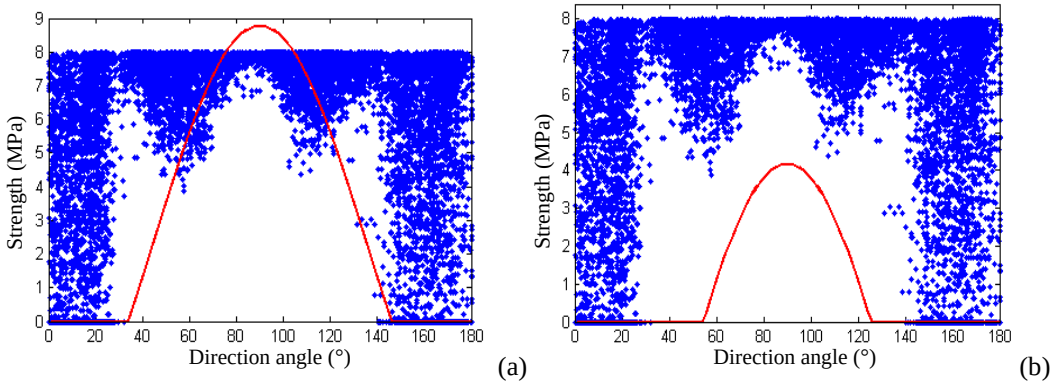


**Fig. 11** Comparison between the residual strength and the critical strength of surrounding rock with the frictional angle: (a) $\varphi = 25.0^{o}$; (b) $\varphi = 27.0^{o}$.

**V.2 Effects of material modulus**

To investigate the effects of material modulus, take the Young's modulus of matrix material $E = 40.0$ GPa, 65.0 GPa, and 90.0 GPa, respectively. The simulation domain is a $50.0\text{m} \times 50.0\text{m} \times 1.0\text{m}$ block (shown in Fig. 12a), which is subjected to the in-situ stresses $S_x = 124.5$ MPa, $S_y = 88.0$ MPa, and $S_z = 111.5$ MPa. The radius of the centered wellbore is $r$=0.1 m. The other parameters

of material properties are: $\nu$=0.2 , $\sigma_t = 4.0$MPa , $C = 10.0$ MPa and $\varphi = 24.0^o$ . Initially, the pressure is imposed on the wall of whole wellbore. The pressurization scheme is shown in Fig. 12b, with $Q_0$=70.0MPa , $Q_p$=115.0MPa , $t_1$=3.0ms and $t_2$=3.1ms . The time step of PF numerical implementation is $\Delta t = 1.0\mu$s . The simulation results of pulsed fracturing are shown in Fig. 13.

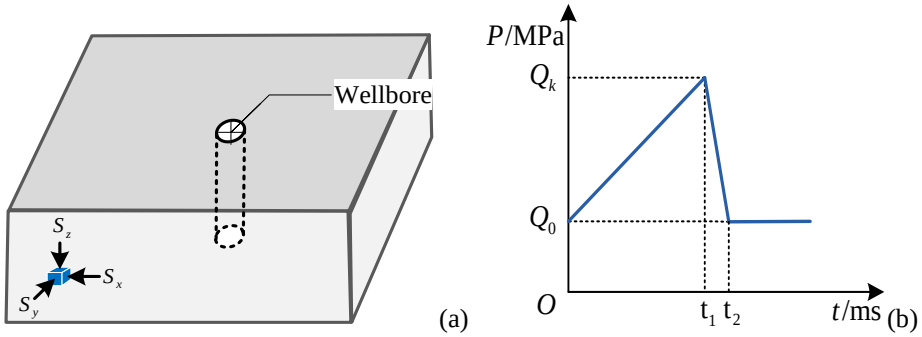


**Fig. 12** Simulation of pulsed fracture: (a) simulation object and boundary condition; (b) pressurization scheme.

Fig. 13 shows the PF simulation results of the case with Young's modulus 65.0 GPa ( $t$=3.1ms ). A symmetrical pulsed fracture is formed at wellbore in the direction of horizontal maximum in-situ stress. Shown in Fig. 14, the damage distribution around wellbore is enlarged with the material modulus increasing. The comparison between residual strength and critical strength of surrounding rock (in Fig. 15) shows that it is potentially dangerous for the wellbore stability. It is found that the unstability risk increases with the material modulus increasing.

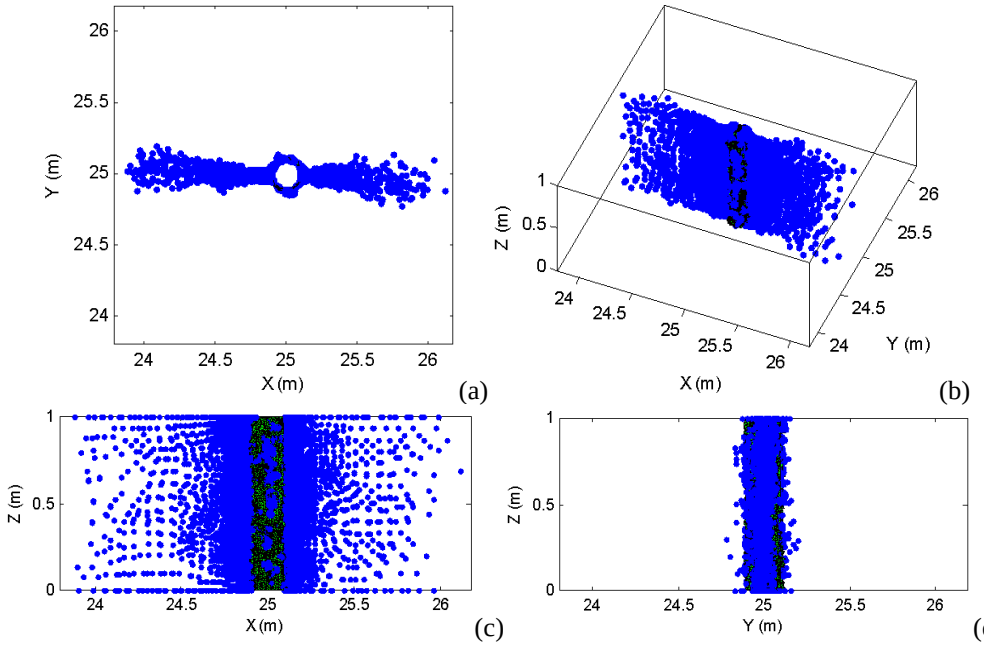


**Fig. 13** Pulsed fracture trajectories viewed from from different directions( $E = 65.0$ GPa , t= 3.1 ms).

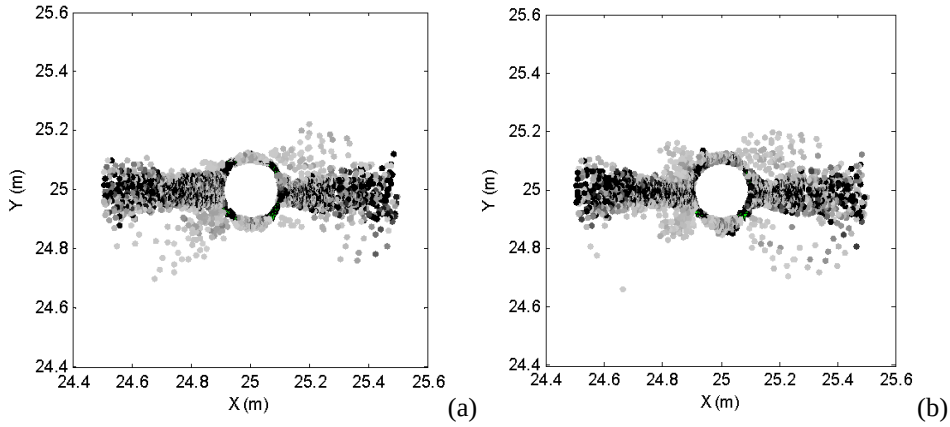

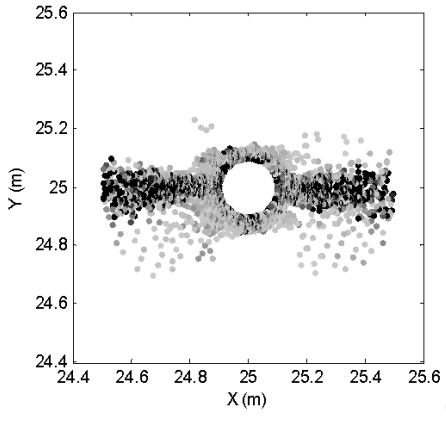


(c)

**Fig. 14** Damage distribution around the wellbore of the cases with material moduli: (a) $E = 40.0$ GPa ; (b) $E = 65.0$ GPa ; (c) $E = 90.0$ GPa (t= 3.1 ms).

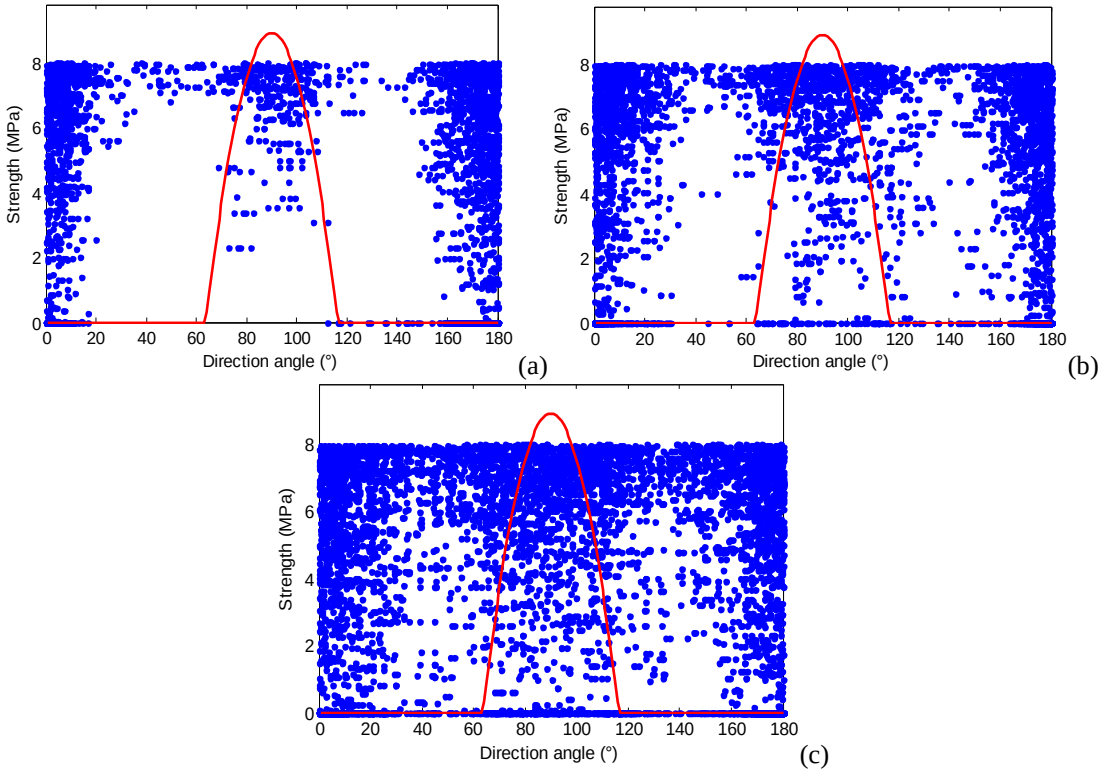


(a) (b) (c)

**Fig. 15** Comparison between the residual strength and the critical strength of surrounding rock with material moduli: (a) $E = 40.0$ GPa ; (b) $E = 65.0$ GPa ; (c) $E = 90.0$ GPa (t= 3.1 ms).

**V.3 Effects of in-situ stresses**

The in-situ stress is an important influence factor in the design of reservoir stimulation. To explore the effect of the in-situ stress on the wellbore stability, we conduct the following simulations with the in-situ stress $S_x/S_y/S_z = 124.5/88.0/111.5$ MPa , $124.5/96.0/111.5$ MPa and $124.5/104.0/111.5$ MPa , respectively. The different in-situ stresses combinations imply different horizontal stress difference. The simulation domain is the same as the cases in Section 5.2. The other simulation parameters are $E = 40.0$ GPa , $\nu$=0.2 , $\sigma_t = 4.0$MPa , $C = 10.0$ MPa and $\varphi = 24.0^o$ . The pressurization scheme shown in Fig. 12b is adopted, with $Q_0$=70.0MPa , $Q_p$=145.0MPa , $t_1$=3.0ms and $t_2$=3.5ms .

Shown in Fig. 16, the simulation results of the case $S_x/S_y/S_z = 124.5/88.0/111.5$ MPa at t= 3.5ms present a symmetric fracture pattern, and there are fracture branches formed on the fracture front. Fig. 17 shows the damage distribution around wellbore. The comparison between residual strength and critical strength of surrounding rock (in Fig. 18) suggests that the dangerous area increases with the horizontal stress difference

increasing. It is suggested that the specific in-situ stresses should be carefully considered in the wellbore stability analysis.

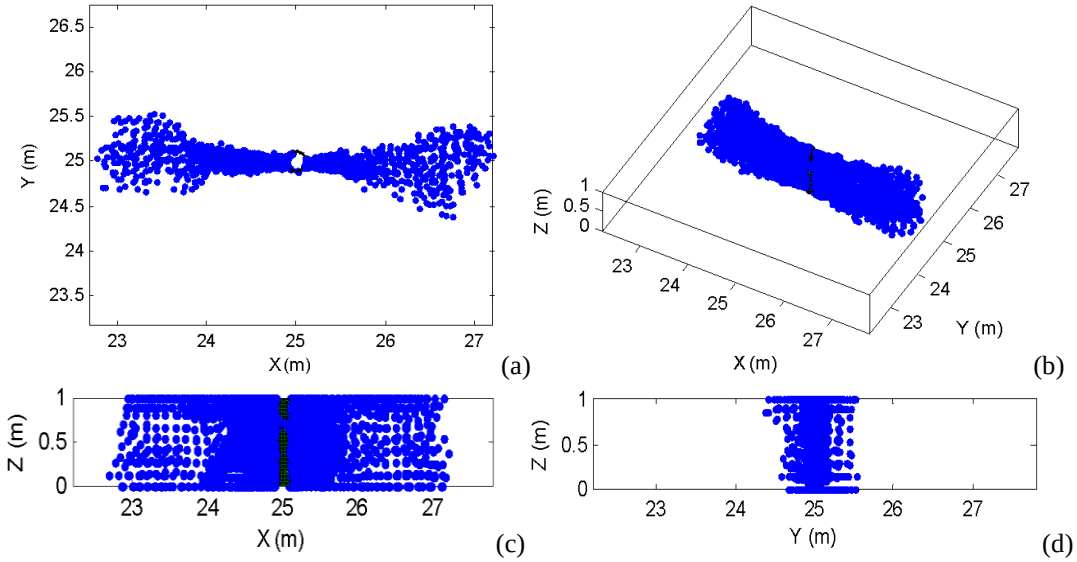


**Fig. 16** Pulsed fracture trajectories in different perspectives of the case $S_x/S_y/S_z = 124.5/88.0/111.5$ MPa (t= 3.5 ms).

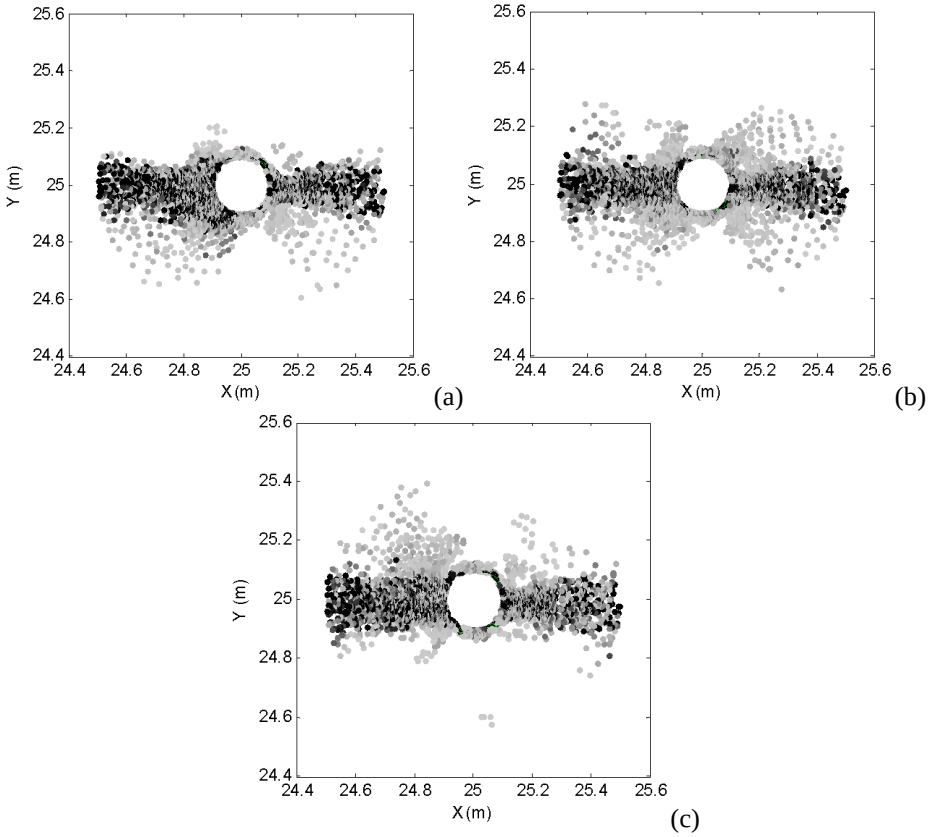


**Fig. 17** Damage distribution around the wellbore of the cases with in-situ stresses: (a) $S_x/S_y/S_z = 124.5/88.0/111.5$ MPa ; (b) $S_x/S_y/S_z = 124.5/96.0/111.5$ MPa ; (c) $S_x/S_y/S_z = 124.5/104.0/111.5$ MPa (t= 3.5 ms).

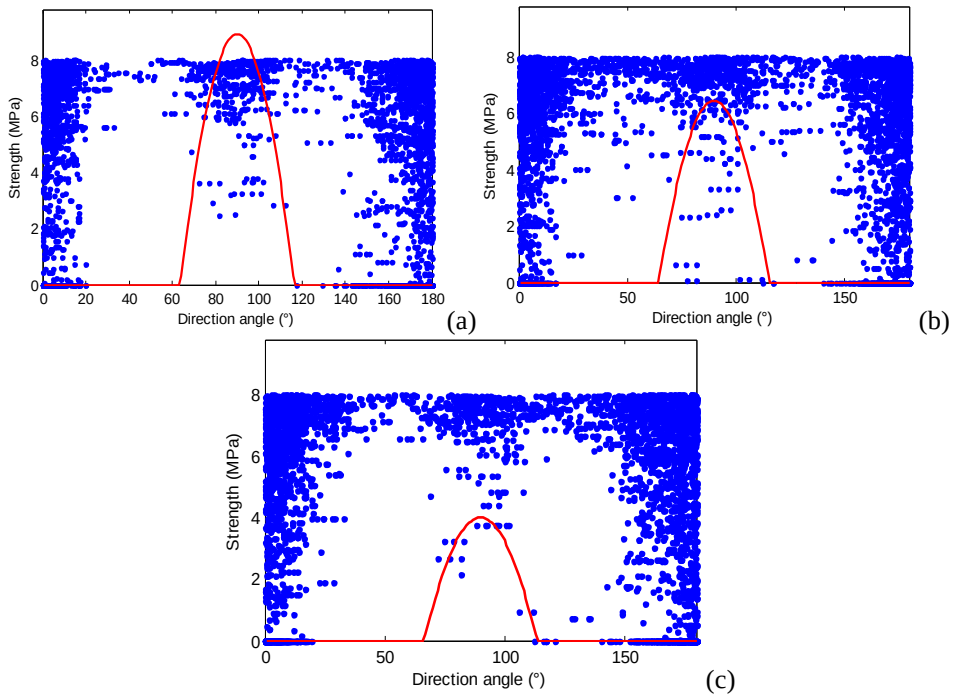


**Fig. 18** Comparison between the residual strength and the critical strength of surrounding rock with in-situ stresses: (a) $S_x/S_y/S_z = 124.5/88.0/111.5$ MPa ; (b) $S_x/S_y/S_z = 124.5/96.0/111.5$ MPa ; (c) $S_x/S_y/S_z = 124.5/104.0/111.5$ MPa (t= 3.5 ms).

**V.4 Effects of pressurization rate**

For the PF stimulation, the various magnitudes of pressurization rates can induce distinct dynamic mechanical responses in the surrounding rock around wellbore. To figure out the influence caused by the pressurization rate, the following simulation is conducted. We take the pressurization rates as $\dot{P} = 20.0$ MPa/ms , 30.0 MPa/ms , and 40.0 MPa/ms , respectively. The simulation domain is a $25.0\text{m} \times 25.0\text{m} \times 0.5\text{m}$ block (shown in Fig. 12a), which is subjected to the in-situ stresses $S_x = 124.5$ MPa , $S_y = 88.0$ MPa , and $S_z = 111.5$ MPa . The other parameters of material properties are: $E = 40.0$ GPa , $\nu$=0.2 , $\sigma_t = 4.0$MPa , $C = 10.0$ MPa and $\varphi = 24.0^{\circ}$ . The pressurization scheme shown in Fig. 12b is adopted, with $Q_0$=70.0MPa , $Q_p$=150.0MPa . For the case $\dot{P} = 20.0$ MPa/ms , $t_1 = 4.0$s and $t_2 = 4.5$s ; for the case $\dot{P} = 30.0$ MPa/ms , $t_1 = 2.67$s and $t_2 = 3.17$s ; for the case $\dot{P} = 40.0$ MPa/ms , $t_1 = 2.0$s and $t_2 = 2.5$s . The peak pressure is a constant in the cases of different pressurization rates.

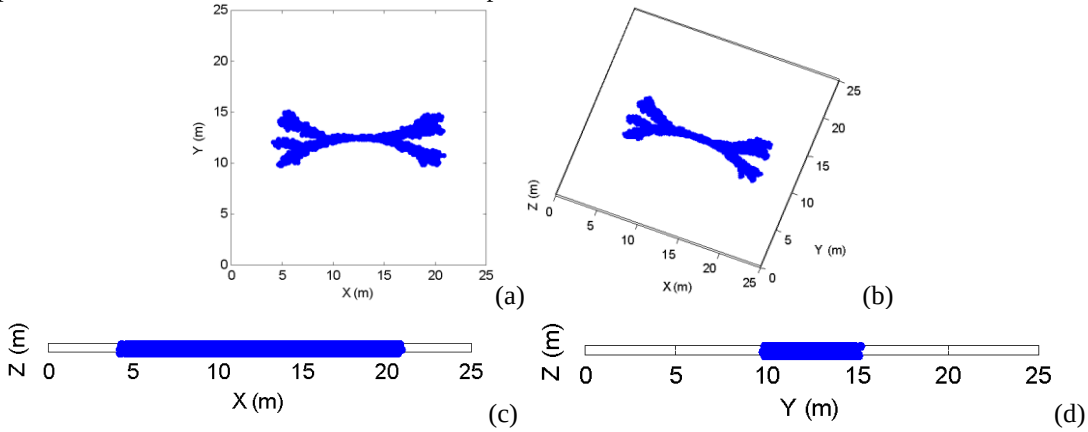


**Fig. 19** Pulsed fracture trajectories in different perspectives of the case $\dot{P} = 20.0$ MPa/ms (t= 4.5 ms).

Fig. 19 shows the simulation results of the case $\dot{P} = 20.0$ MPa/ms at the time t= 4.5ms. A symmetrical pulsed fracture is formed at wellbore in the direction of horizontal maximum in-situ stress. It is found that the

pulsed fractures branch under the pulse pressurization, which form a complex fracture network in reservoir. Seen from Fig. 20, the damage area is decreased with the pressurization rate's increasing. The comparison between residual strength and critical strength of surrounding rock (in Fig. 21) suggests that the dangerous area is decreased with the pressurization rate increasing. It implies that, to some degree, the high pressurization rate is more helpful to maintain the wellbore stability. In other word, when the peak pressure keeps constant, the pressurization time dominates the wellbore stability. So it is crucial to choose reasonable pressurization rate and pressurization time in the PF practice.

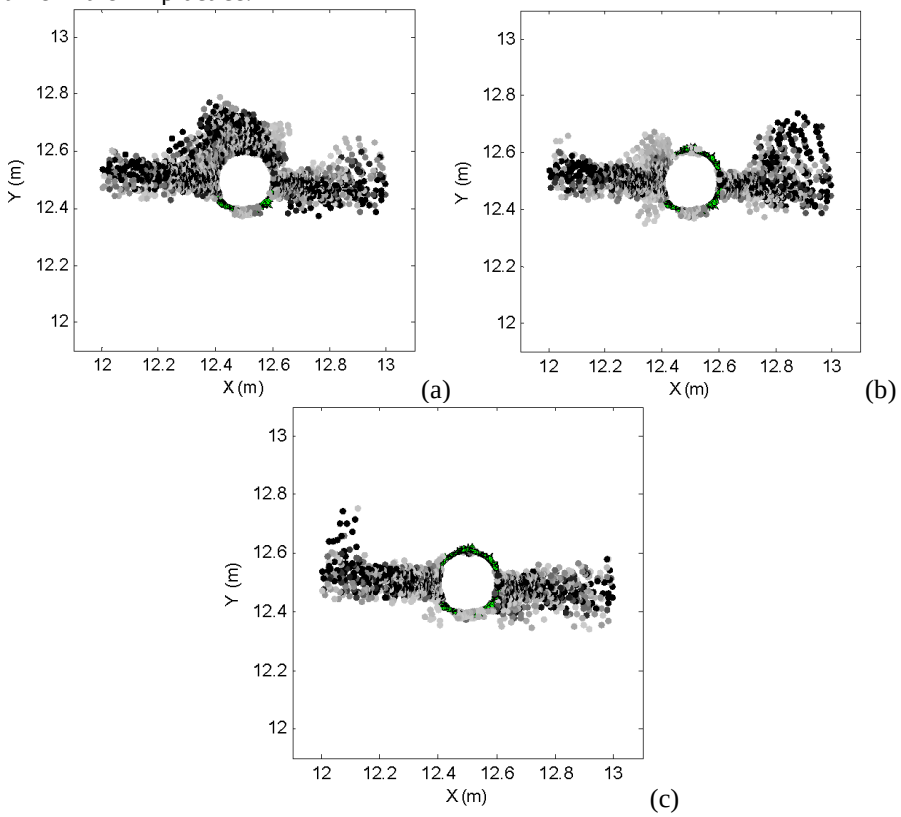


**Fig. 20** Damage distribution around the wellbore of the cases with pressurization rates: (a) $\dot{P} = 20.0$ MPa/ms (t= 4.5 ms); (b) $\dot{P} = 30.0$ MPa/ms (t= 3.2 ms); (c) $\dot{P} = 40.0$ MPa/ms (t= 2.5 ms).

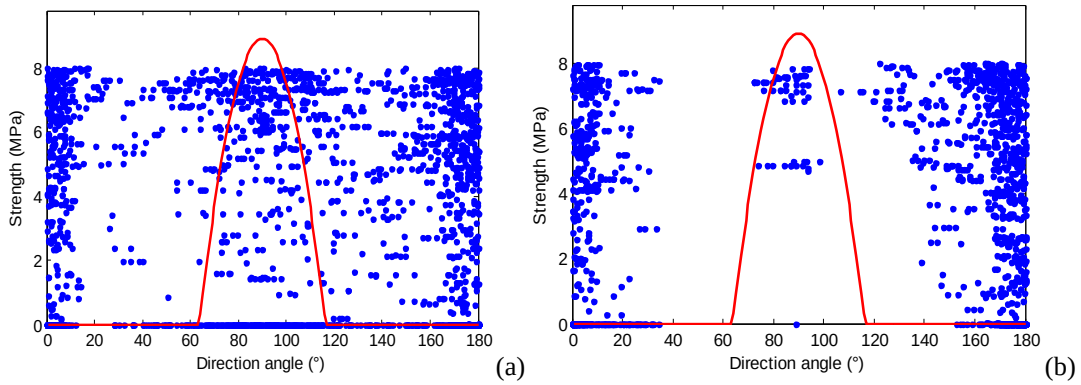

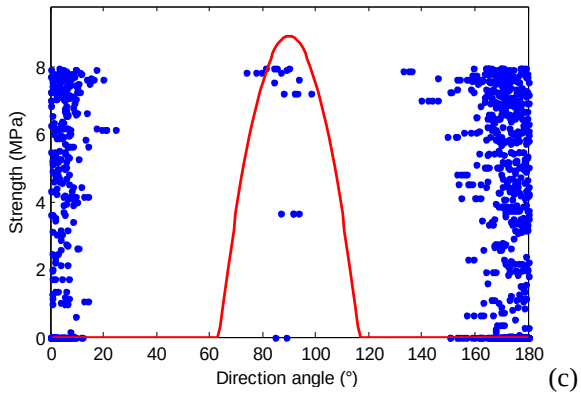


(c)

**Fig. 21** Comparison between the residual strength and the critical strength of surrounding rock with pressurization rates: (a) $\dot{P} = 20.0$ MPa/ms (t= 4.5 ms); (b) $\dot{P} = 30.0$ MPa/ms (t= 3.2 ms); (c) $\dot{P} = 40.0$ MPa/ms (t= 2.5 ms).

## VI. CONCLUSIONS

In this paper, an assessment method is developed for the wellbore stability after PF stimulation based on the numerical analysis. The AVIB is adopted to model the reservoir matrix. Based on the numerical simulation results, the residual strength of surrounding rock is calculated through the damage factor derived from the element state. The Mohr-Coulomb criterion is used to characterize the critical strength of surrounding rock. Through the comparison between the residual strength and the critical strength of surrounding rock, the risk of wellbore instability is recognized.

The simulation results suggest that the internal friction angle of matrix material has a significant effect on the wellbore stability. The larger the internal friction angle is, the safer the wellbore is. It is found that the dangerous area increases with the material modulus increasing. The dangerous area gets larger with the horizontal in-situ stress difference increasing. When the peak value of the pulse pressure is fixed, the high pressurization rate is more helpful to maintain the wellbore stability, in which the pressurization time has an important impact on the wellbore stability. The present method provides a simple and effective approach for wellbore stability assessment after PF stimulation.

## ACKNOWLEDGEMENT

The present work is supported by the National Science and Technology Major Projects (No. 2016ZX05014-005-005), which is gratefully acknowledged.

## REFERENCES

[1]. Kang Y. Characteristics and distribution laws of paleokarst hydrocarbon reservoirs in palaeozoic carbonate formations in China. Natural Gas Industry 2008;28(6):1-12. (In Chinese)
[2]. Li Y. Development theories and methods of fracture-vug carbonate reservoirs. Elsevier: Academic Press. 2017:1-116.
[3]. Mody RK, Coronado MP. Multilateral wells: Maximizing well productivity. In: Davies M., Lumsden A., Kline W., Kakadiaris I. (eds) Pumps and Pipes. Springer, Boston, MA. 2011.
[4]. Kalfayan LJ. Fracture acidizing: History, present state, and future. Society of Petroleum Engineers, 2007, January 1. doi:10.2118/106371-MS.
[5]. Nino-Penaloza A, Gomaa AM. New insights on chemical diversion in carbonate acidizing: Experimental and simulation-based study. Society of Petroleum Engineers. 2016, September 26. doi:10.2118/181485-MS.
[6]. Benavides SP, Myers WD, Van Sickle EW, Vargervik K. Advances in horizontal oriented perforating. Society of Petroleum Engineers. 2003, January 1. doi:10.2118/81051-MS.
[7]. Norouzi P, Hashemolhosseini H, Baghbanan A. Stress-dependent perforation in carbonate rocks: An experimental study. Society of Petroleum Engineers. 2018, September 1. doi:10.2118/191140-PA
[8]. Salazar A, Almanza E, Chira P, Folse K. Application of propellant high-energy gas fracturing in gas-injector wells at El Furrial field in northern Monagas state - Venezuela. In: Proceedings of the SPE International Symposium and Exhibition on Formation Damage Control. Lafayette, Louisiana. 20-21 February 2002; SPE 73756.
[9]. Jaimes MG, Castillo RD, Mendoza SA. High energy gas fracturing: A technique of hydraulic prefracturing to reduce the pressure losses by friction in the near wellbore - a Colombian field application. In: Proceedings of the SPE Latin American and Caribbean Petroleum Engineering Conference. Mexico City, Mexico. 16-18 April 2012; SPE 152886.
[10]. Al-Nakhli AR. Chemically-induced pressure pulse: A new fracturing technology for unconventional reservoirs. In: Proceedings of the SPE Middle East Oil & Gas Show and Conference. Manama, Bahrain. 8-11 March 2015; SPE-172551-MS.
[11]. Tariq Z, Mahmoud M, Abdulraheem A, Al-Nakhli A, Bataweel M. A review of pulse fracturing treatment: An emerging stimulation technique for unconventional reservoirs. Society of Petroleum Engineers. 2019, March 15. doi:10.2118/194870-MS.
[12]. Zhang ZN, Peng SJ, Ghassemi A, Ge XR. Simulation of complex hydraulic fracture generation in reservoir stimulation. J Petrol Sci Eng 2016;146:272-285.
[13]. Liu Z, Peng S, Zhao H, Geng Y, Zhang Z. Numerical simulation of pulsed fracture in reservoir by using discretized virtual internal

bond. J Petrol Sci Eng 2019;181:106197.
[14]. Wang YJ, Zhao B, He XB, Zhang ZN. 3D pulsed fracture initiation and propagation around wellbore: A numerical study. Comput Geotech 2020;119:103374.
[15]. Gao Jordan, Odunlami T, Osayande N. Shale bedding impact on wellbore stability and drilling optimization. SPE/CSUR Unconventional Resources Conference. Calgary, Alberta, Canada. 30 September - 2 October 2014; SPE-171601-MS.
[16]. Lu YH, Chen M, Jin Y, Zhang GQ. A mechanical model of borehole stability for weak plane formation under porous flow. Petroleum Science and Technology, 2012;30(15):1629-1638.
[17]. Ma T, Chen P. A wellbore stability analysis model with chemical-mechanical coupling for shale gas reservoirs. Journal of Natural Gas Science & Engineering, 2015;26:72-98.
[18]. Braun R. A commonly neglected factor in rock mass and borehole stability. Oil Gas European Magazine 2007;33(2):79-82.
[19]. Holt RM, Fjær RE, StenebråTen JF, Nes OM. Brittleness of shales: Relevance to borehole collapse and hydraulic fracturing. J Petrol Sci Eng 2015;131:200-209.
[20]. Carcione JM, Helle HB, Gangi AF. Theory of borehole stability when drilling through salt formations. Geophysics 2006;71(3):31-47.
[21]. Zhang ZN, Gao HJ. Simulating fracture propagation in rock and concrete by an augmented virtual internal bond method. Int J Numer Anal Meth Geomech 2012;36:459-482.
[22]. Gao HJ, Klein P. Numerical simulation of crack growth in an isotropic solid with randomized internal cohesive bond. J Mech Phys Solids 1998;46:187-218.
[23]. Xu XP, Needleman A. Void nucleation by inclusion debonding in a crystal matrix. Modelling Simul Mater Sci Eng 1993;1:111-132.
[24]. Xu XP, Needleman A. Numerical simulations of fast crack growth in brittle solids. J Mech Phys Solids 1994;42:1397-1434.
[25]. Lu W, Tao Z. A study on fracture propagation velocity driven by gases of explosion products. Explosion Shock Waves 1994;14(3):264-8. (In Chinese)
[26]. Kirsch G. Die theorie der elastizitat und die bedurfnisse der festigkeitslehre. Verein Deutsher Ingenieure 1898;42(28):797-807.

Xinyong Li, et. al. "Assessment of Borehole Stability after Pulsed Fracture ." *International Journal of Engineering Research And Development*, vol. 16(4), 2020, pp 28-41.